Available online at www.sciencedirect.com

ScienceDirect

Ceramics International 40 (2014) 723–728

CERAMICS INTERNATIONAL

www.elsevier.com/locate/ceramint

Catalytic conversion of syngas to olefins over Mn–Fe catalysts

Saleh A. Al-Sayari[a,b,*]

[a]Advanced Materials and NanoResearch Center, Najran University, P.O. Box 1988, Najran 11001, Saudi Arabia
[b]Chemistry Department, Faulty of Science and Art at Sharurah, Najran University, Saudi Arabia

Received 2 June 2013; received in revised form 16 June 2013; accepted 17 June 2013
Available online 24 June 2013

Abstract

A series of MnO_2–Fe_2O_3 with various contents of Mn (0–40% atomic ratio) was synthesized by the co-precipitation method. XRD patterns indicate that the sharp and intense peaks are related to the excellent crystal quality of α-Fe_2O_3 nanostructures. HR-TEM images showed that α-Fe_2O_3 and MnO_2, were partly in close contact and the lattice fringes exhibit the typical distances, i.e., α-Fe_2O_3 (104) (2.7 Å) and MnO_2 (310) (3.1 Å). X-ray photoelectron spectroscopy (XPS) results of the Fe 2p core-level binding energy spectrum of the α-Fe_2O_3 and Mn 2p, indicated the presence of Fe^{3+} and Mn^{4+}. The direct synthesis of olefins from syngas was carried out over the MnO_2–Fe_2O_3 catalysts under pressurized fixed-bed continuous flow conditions. The results showed that Mn–Fe catalyst had high catalytic activity and high olefins selectivity without the addition of any promoters at low pressure. It was found that the catalyst containing 20 at% Mn–Fe was an optimal catalyst for the conversion of synthesis gas to hydrocarbons especially light olefins. The maximum CO conversion rate was 15%, and the yield of olefins (totally about 23.77%) with a predominance of CH_4 (12.24%), and C_2H_6 (2.80%) components. Mn–Fe catalyst can be regarded as a potential candidate for catalytic conversion of biomass-derived syngas to olefins.

Keywords: Conversion; Syngas; Olefins; Mn–Fe catalysts

1. Introduction

The world today is seeking a fossil fuel for energy demand. In near future, the petroleum energy will be finite and depleted. There are several important issues need to be addressed regarding the energy problems, such as high need for energy, high depletion of nonrenewable energy resources, high local and global environmental pollution [1]. The conversion of syngas to olefins has been considered as a possible solution to meet the growing demands for chemical feedstocks such as ethylene, propylene and butylene. The production of light alkenes calls for the development of new catalysts to achieve high activity, selectivity and stability. Much attention has been paid to the development of catalysts for light olefin synthesis from CO hydrogenation, and some distinct improvements have been achieved in recent years [1]. Among the reported catalysts, iron-based catalysts are promising in the selective synthesis of light olefins from CO hydrogenation [2–5]. Potassium and manganese oxides have been found to be the most efficient promoters among all studied additives so far [6]. Extensive investigations have been conducted on iron–manganese catalysts that produced more C2–C4 olefins with lower CH_4 selectivity than other catalysts over a wide range of reaction temperature and H_2/CO ratio [7–21]. In addition to the active metal the catalysts typically contain a number of 'promoters' including potassium and copper. Group 1 alkali metals, including potassium, are poison for cobalt catalysts but are promoters for iron catalysts. The promoters are playing an important role and they are considered the key factors on activity and selectivity. In this contribution, the crystalline structure and catalytic performance of a series of Mn–Fe with various contents of Mn (0–40% atomic ratio) was synthesized by the co-precipitation method. The catalysts were investigated under model syngas evaluation and some significant results were obtained. The results showed that Mn–Fe catalyst had high catalytic activity and high olefins selectivity without addition of any promoters at low pressure. The maximum CO

*Corresponding author at: Advanced Materials and NanoResearch Center, Najran University, P.O. Box 1988, Najran 11001, Saudi Arabia.
Tel.: +966 75428888; fax: +966 75428887.
E-mail address: Salehalsayari8@gmail.com

0272-8842/$ - see front matter © 2013 Elsevier Ltd and Techna Group S.r.l. All rights reserved.
http://dx.doi.org/10.1016/j.ceramint.2013.06.061

conversion rate was 15%, and the yield of olefins (totally about 23.77%) with a predominance of CH_4 (12.24%), and C_2H_6 (2.80%) components. Mn–Fe catalyst can be regarded as a potential candidate for catalytic conversion of biomass-derived syngas to olefins.

2. Experimental details

2.1. Materials and catalysts synthesis

$Mn(NO_3)_2 \cdot 4H_2O$, $Fe(NO_3)_3 \cdot 9H_2O$ and ammonium hydroxide were purchased from Sigma-Aldrich. Mn–Fe oxides catalysts at different Mn contents 5, 10, 15, 20 and 40 atomic ratio were prepared by the co-precipitation method, using ammonium hydroxide as a precipitant. In this process, aqueous solutions of $Mn(NO_3)_2 \cdot 4H_2O$, $Fe(NO_3)_3 \cdot 9H_2O$ (1 mol/l) were premixed in a round bottom flask and the resulting solution was heated at 80 °C with strong stirring. Ammonium hydroxide solution (5.6 M) was added to the mixed nitrate solution, which was continuously stirred at 80 °C. pH was raised from 2.80 to 9.0 and then kept half an hour for ageing under stirring at the same temperature. The precipitates were first filtered and then washed several times with warm distilled water. The precipitates were then dried at 110 °C for 16 h and subsequently calcined in static air in the furnace at 550 °C for 16 h to obtain the final catalyst.

2.2. Characterization

Transmission electron microscopy (TEM) was conducted at 200 kV with a JEOL JEM-2100F-UHR field-emission instrument equipped with a Gatan GIF 2001 energy filter and a 1 k-CCD camera in order to obtain EEL spectra. Field emission-secondary electron microscope (FE-SEM) images were carried out with a FE scanning electron microanalyzer (JEOL-6300F; 5 kV). X-ray diffraction (XRD) data were acquired on a PANalytical X′pert diffractometer using Cu $K\alpha_{1/2}$, $\lambda\alpha_1$= 154.060 pm, $\lambda\alpha_2$=154.439 pm radiation. X-ray photoelectron spectroscopy (XPS) was used to study the chemical composition of the catalyst surfaces. Photoelectron spectra were recorded with a VG Escalab 200R electron spectrometer equipped with a Mg Kα X-ray source ($h\nu$=1253.6 eV) and a hemispherical electron analyzer operating at constant transmission energy (20 eV). The O 1s, Mn 2p, and Fe 2p core-level spectra were recorded and the corresponding binding energies were referenced to the C 1s line at 284.6 eV (accuracy within 0.1 eV).

2.3. Catalytic test

Prior to the catalytic test, the catalysts must be activated in order to reduce the Fe and Mn particles. Therefore, the samples synthesized as described above (as-prepared samples) were treated under a flow of H_2 (10 vol%) for 1.5 h at 823 K (H_2-reduced samples). The catalytic activity tests of the catalyst samples were performed in a pressurized integral fixed bed flow reactor and the reaction conditions were held constant at the following conditions: catalyst 1 g, CO/H_2=1:3 (molar feed ratio), a gas hourly space velocity (GHSV)=1000 h^{-1}, total pressure=1 atm., T=573 K. Higher pressures would be favorable, but the benefits may not justify the additional costs of high-pressure equipment, and higher pressures can lead to catalyst deactivation via coke formation. The feed gas and the products were all analyzed using gas chromatograph. The analysis of gas phase product has been carried out with an on-line Agilent 7890 gas chromatograph provided with two thermal conductivity detectors (TCD) and a flame ionization detector (FID). Helium and nitrogen were used as the carrier gases. Liquid products were collected using a condenser kept at −3 °C. Liquid samples were analyzed using an Agilent 7683B Series Injector coupled to an Agilent 6890 Series gas chromatograph system and a 5973 Mass Selective Detector. The results were presented in terms of activity by CO conversion (Xco), light olefin selectivity by olefin to paraffin ratio (O/P) in the C2–C4 fraction. CH_4 and CO_2 selectivity by molar percentage of CO converted to CH_4 and CO_2 in total CO converted, and the hydrocarbon distribution was expressed as the weight percentage of desired components in all hydrocarbons. Mass balance and carbon balance were performed based on inlet/outlet flows, gas composition analysis and liquid product weight and composition.

3. Results and discussion

3.1. Structural investigations

The XRD patterns of the pure α-Fe_2O_3 and MnO_2/α-Fe_2O_3 at different Mn atomic ratios 5% (b), 10% (c), 15% (d), 20% (e) and 40% (f) calcined at 550 °C for 16 h are shown in Fig. 1. All of the diffraction peaks can be indexed as hexagonal α-Fe_2O_3 with lattice constants a=5.035 Å and c=13.74 Å, in agreement with the reference values of JCPDS (no. 33-0664) and the calculated 'd' values are in good agreement with the standard 'd' values. The well-defined diffraction peaks possess

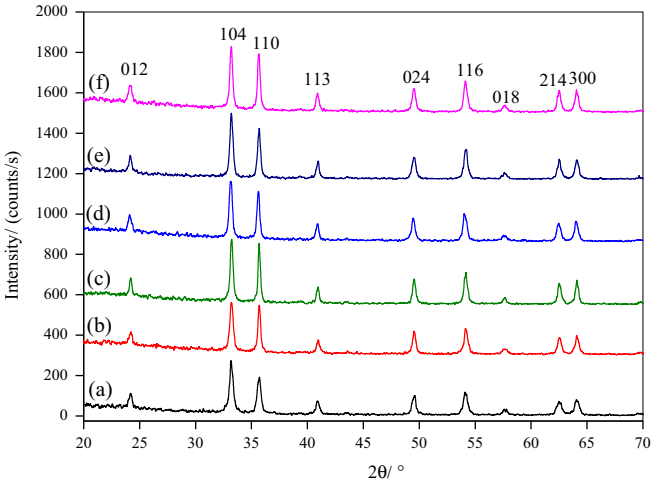

Fig. 1. XRD of pure α-Fe_2O_3 (a) and MnO_2/α-Fe_2O_3 at different Mn atomic ratios 5% (b), 10% (c), 15 (d), 20% (e) and 40% (f) calcined at 550 °C for 16 h. Shifted for sake of clarity.

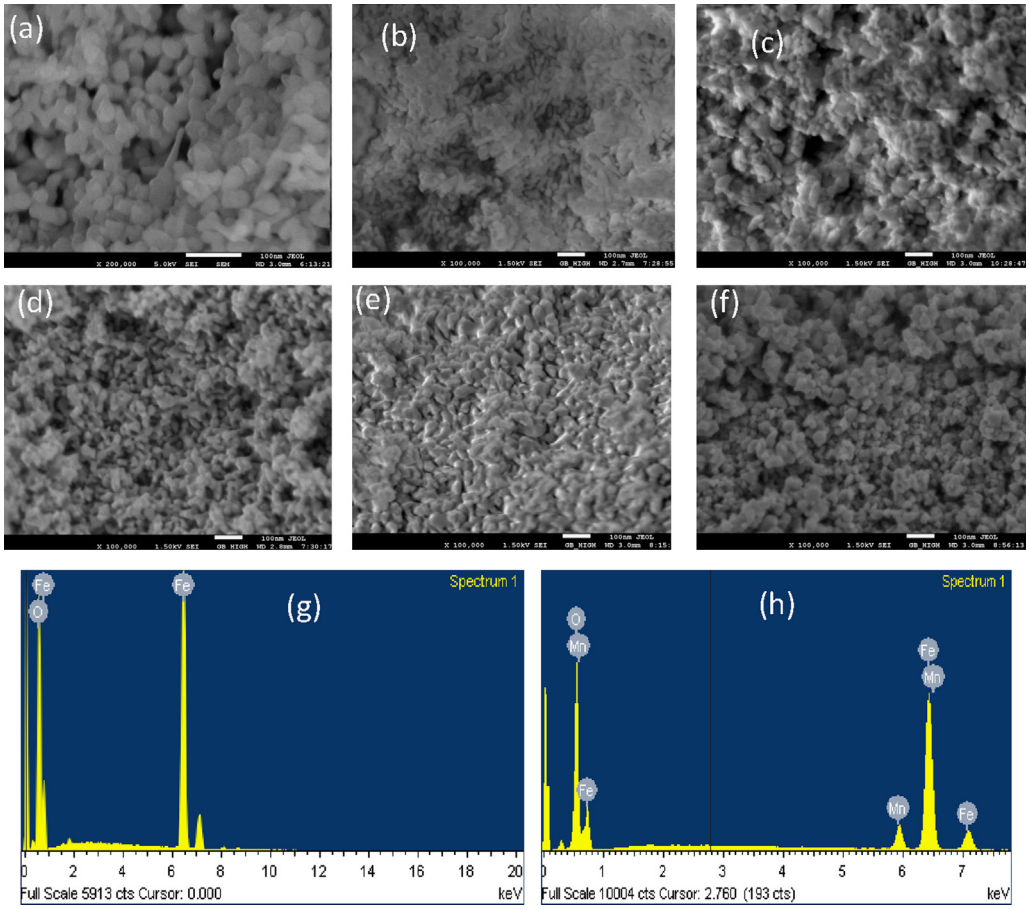

Fig. 2. FE-SEM images of pure α-Fe_2O_3 (a) and MnO_2/α-Fe_2O_3 at different Mn atomic ratios 5% (b), 10% (c), 15% (d), 20% (e) and 40% (f) calcined at 550 °C for 16 h. Energy dispersion spectrum (EDS) analysis of pure α-Fe_2O_3 (g) and 20% MnO_2/α-Fe_2O_3 (h).

orientations in the (012), (104), (110), (113), (024), (116), (018), (214), and (300) planes [22]. The peak intensity of the (104) diffraction peak in the XRD patterns was relatively higher than the other peaks. Thus the enhanced peak intensity of (104) indicates that α-Fe_2O_3 exhibits highly crystalline structure. The sharp and intense peaks in the spectrum indicated the excellent crystal quality of α-Fe_2O_3 nanostructures. The average crystallite size of α-Fe_2O_3 was calculated by using Scherrer's equation. It is observed that the average crystallite size was ranging from 20 nm to 30 nm, calculated from the Scherrer's formula.

FE-SEM images of pure α-Fe_2O_3 (a) and MnO_2/α-Fe_2O_3 at different Mn atomic ratios 5% (b), 10% (c), 15% (d), 20% (e) and 40% (f) calcined at 550 °C for 16 h are shown in Fig. 2. The pure Fe_2O_3 showed relatively uniform and spherical particles with size of about 20 nm, whereas with increasing Mn content, as shown in Fig. 3b–e, revealed that a little bit granular aggregates of particles distributed in irregular shapes, scallop shells-like (Fig. 2e) and they have a porous structure on the surfaces, which could be used for the adsorption of syngas. At 40% Mn, it is regular and spherical particles with size of 30 nm. Energy dispersive X-ray spectra (EDXS) indicate the presence of Fe and Mn (Fig. 2g and h) with no contamination, confirming the high purity of catalysts. The final Fe and Mn contents in the prepared samples are consistent with the Mn:Fe ratio used in the starting mixtures.

TEM images of the pure α-Fe_2O_3 (a) and 20 at% Mn/α-Fe_2O_3 (c) were shown in Fig. 3. An overview image of α-Fe_2O_3 and 20 at% Mn/α-Fe_2O_3 at low magnification illustrates that the product is almost exclusively composed of discrete α-Fe_2O_3 nanoparticles agglomerated. Although it is rather difficult to observe the grain boundaries clearly, it can be said that the particles are quite uniform in size and shape (Fig. 3a and c). Both, the HRTEM image (Fig. 3b and d) and the selective area electron diffraction (SAED, inset Fig. 3b) show well resolved (104) lattice fringes (distance: 0.27 nm) and the observed is a diffraction indicative of a highly crystalline α-Fe_2O_3 framework. The HRTEM image Fig. 3d of synthesized 20 at% Mn/α-Fe_2O_3 nanostructure shows the lattice fringe pattern of MnO_2 nanostructure, the interplanar spacing is about 0.31 nm, which corresponds to the separation between (310) lattice planes of MnO_2. Both sorts of nanoparticles, α-Fe_2O_3 and MnO_2, are partly in close contact as seen most impressively in Fig. 3d; the lattice fringes exhibit the typical distances, i.e., α-Fe_2O_3 (104) (2.7 Å) and MnO_2 (310) (3.1 Å).

The binding energies of core-electrons Mn 2p, Fe 2p, and O 1s have been recorded for the as-prepared catalysts by X-ray photoelectron spectroscopy (XPS) and the results are summarized

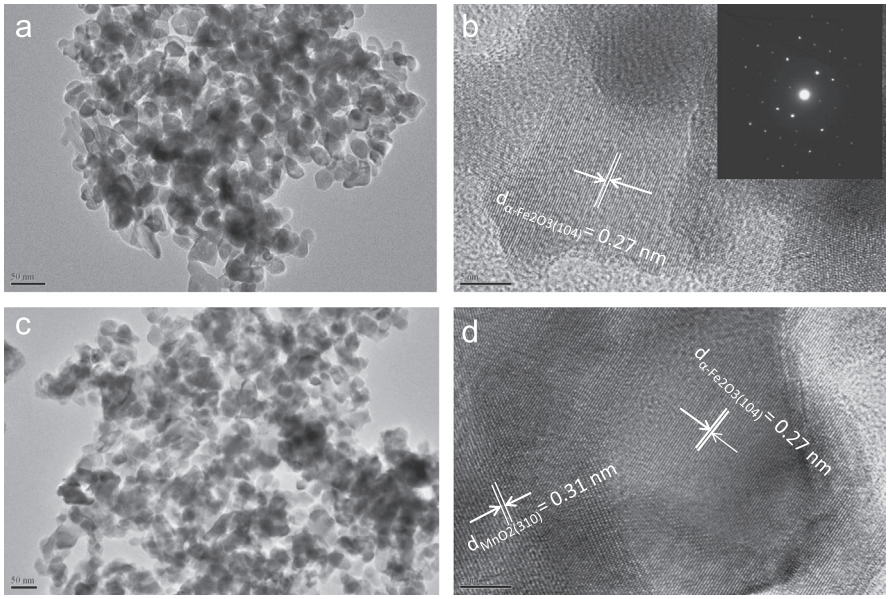

Fig. 3. TEM images of pure α-Fe_2O_3 (a) and 20 at% Mn/α-Fe_2O_3 (c). HRTEM image of pure α-Fe_2O_3 (b) and 20 at% Mn/α-Fe_2O_3 (d). Selective area electron diffraction (SAED, inset Fig. 3b) show well resolved lattice fringes of α-Fe_2O_3.

Table 1
Binding energies (eV) of core levels of Mn(x)/Fe catalysts.

Mn (%)	Fe $2p_{3/2}$	Mn $2p_{3/2}$	O1s
0	710.9	–	530.3 (79)
			531.7 (21)
5	710.3 (70)	541.9	529.7 (77)
	711.6 (30)		531.5 (23)
10	710.2 (74)	542	529.7 (81)
	711.6 (26)		531.5 (19)
15	710.3 (57)	542	529.7 (80)
	711.5(43)		531.4 (19)
20	710.4 (68)	542	529.7 (84)
	711.6 (32)		531.5 (16)
40	710.1 (45)	541.7	529.6 (83)
	711.6 (55)		531.2 (17)

in Table 1 and Fig. 4. Fig. 4(a) shows the Fe 2p core-level binding energy spectrum of the α-Fe_2O_3. The fitting peaks at around 711 and 724 eV are assigned to Fe $2p_{3/2}$ and Fe $2p_{1/2}$ peaks, respectively. The 711 eV binding energy of Fe $2p_{3/2}$, the 13 eV difference between Fe $2p_{3/2}$ and Fe $2p_{1/2}$ peaks and the presence of a satellite peak located at about 718 eV are characteristics of Fe^{3+} state. This value is characteristic of Fe^{3+} state indicating the formation of the α-Fe_2O_3 by the experimental methodology used [23,24]. The binding energy interval corresponding to Mn $2p_{1/2}$ and Mn $2p_{3/2}$ peaks were analyzed by XPS. Fig. 4b and c shows Mn $2p_{1/2}$ and Mn $2p_{3/2}$ peaks normalized spectra of Mn–Fe oxide samples prepared at different Mn contents 10 and 20 at%. In this case we can see that all spectra look quite similar and no big differences are observed due to Mn contents (Table 1). Only the spectrum corresponding to the manganese oxide sample shows the peak slightly shifted toward lower binding energies. In all cases the measured binding energy for Mn $2p_{3/2}$ and Mn $2p_{1/2}$ transitions centered at 641.65 and 653.45 eV respectively having spin energy separation of 11.80 eV in the present work with the values available in the literature, indicated the presence of manganese as Mn^{4+} [25–27] which is consistent with the oxidation state of Mn in MnO_2. The O 1s peak appeared symmetric with a binding energy of 529.7–531.7 eV (Table 1). For pure α-Fe_2O_3 sample, the dominant peak located at 530.30 eV corresponds to the oxygen bonded as α-Fe_2O_3. However, after Mn addition, the deconvoluted O 1s spectrum (Fig. 4d) is deconvoluted into two peaks at 529.7 and 531.5 eV, which are in good agreement with the literature values of α-Fe_2O_3 [28,29]. The Fe 2p and O 1s spectra indicate that the valence states of elements Fe and O are +3 and −2, respectively.

3.2. Catalytic investigation

To explore the influence of Mn percentage into Fe on the catalytic performance, the catalytic performances of the catalysts are shown in Fig. 5 and summarized in Table 2. All these different supported catalysts were tested under the same reaction conditions ($H_2/CO = 3/1$, GHSV = 1000 h^{-1}, $P = 1$ atm at 573 K). The carbon balance for all the reactions was set between 95% and 102%. The Fe_2O_3 sample showed lower activity than the other samples. It could be seen that the activities of the catalysts showed significant changes after Mn addition. They reveal that the selectivity increases with increasing Mn content up to 20 at% Mn–Fe. Subsequently, the selectivity gradually decreases with increasing Mn/Fe atomic ratio. At 20% Mn sample, one could observe high olefin selectivity and also high CH_4 selectivity, Table 2 shows typical liquid product fuels obtained with the catalyst. In general, it was observed that the main reaction products were olefins (totally about 23.77%) with a predominance of CH_4 (12.24%), and C_2H_6 (2.80%) components. However, the olefin selectivity was the highest and the CH_4 selectivity was the lowest on 40% Mn sample. It could also be seen that the samples pretreated by syngas at 553 K were preferable to

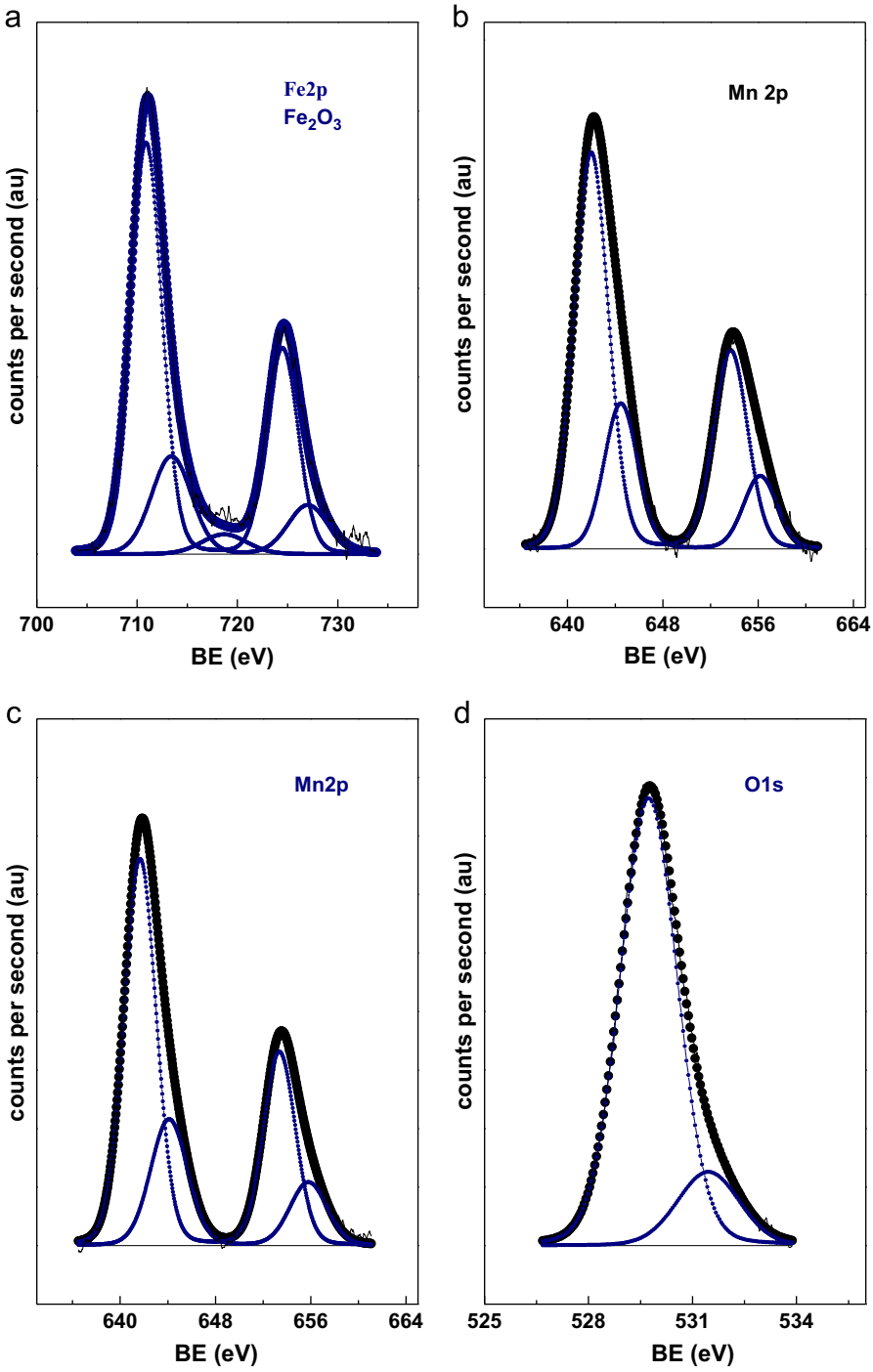

Fig. 4. XPS Fe 2p, Mn 2p and O1s spectra of prepared catalysts.

produce heavier hydrocarbons, which would be caused by strong CO adsorption and dissociation ability. However, CO pretreated at low temperature and H_2 pretreated samples favored the formation of light hydrocarbons. The changes of catalytic performances showed great relations with CO adsorption. Mn–Fe bimetallic nanocatalysts were found to enhance the CO conversion. Incorporation of Mn into Fe nanocatalyst led to better reducibility and higher H_2-consumption which would have resulted in more metal active sites available. Thus, it enhanced catalytic activity compared to those of the monometallic nanocatalysts [30]. In general, it was found that the catalyst containing 20 at% Mn–Fe was an optimal catalyst for the conversion of synthesis gas to hydrocarbons especially light olefins.

4. Conclusions

A series of MnO_2–Fe_2O_3 with various contents of Mn (0–40% atomic ratio) was synthesized by the co-precipitation method. XRD results indicated that the sharp and intense peaks

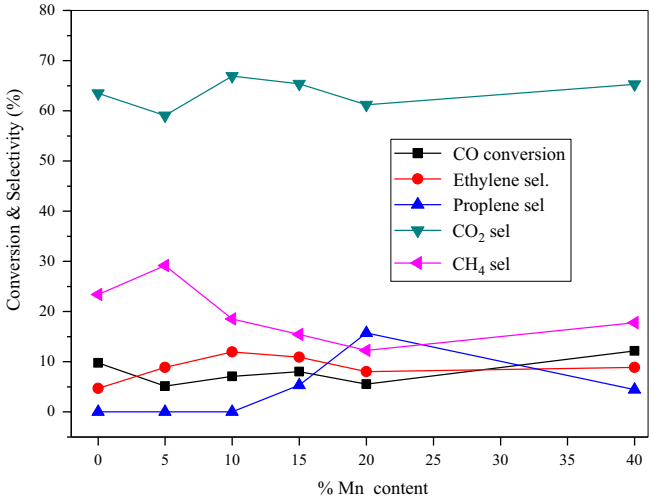

Fig. 5. Effect of Mn content on stream of CO conversion, Ethylene selectivity, Propylene selectivity, CO_2 selectivity and CH_4 selectivity distribution on MnO_2–Fe_2O_3 catalyst at the reaction condition of 0.1 MPa, 573 K, with syngas of $CO/H_2 = 1:3$.

Table 2
Effect of Mn content on catalytic performance of the admixed catalyst of MnO_2–Fe_2O_3.

Mn (%)	CO conversion (%)	Selectivity (%)				
		Ethylene	Propylene	CO_2	CH_4	C_2H_6
0	9.97	4.68	0	63.47	23.39	1.78
5	5.17	8.86	0	59.04	29.15	2.95
10	7.1	11.96	0	66.91	18.51	2.62
15	8.02	10.94	5.35	65.4	15.46	2.85
20	5.53	8.04	15.73	61.19	12.24	2.8
40	12.16	8.9	4.45	65.28	17.8	3.65

in the spectrum indicated the excellent crystal quality of α-Fe_2O_3 nanostructures. TEM showed that Mn/α-Fe_2O_3 illustrates that the product is almost exclusively composed of discrete α-Fe_2O_3 nanoparticles agglomerated and the particles are quite uniform in size and shape. The HRTEM image of synthesized 20 at% Mn/α-Fe_2O_3 nanostructure shows the lattice fringe pattern of Fe_2O_3 and MnO_2 nanostructure, the interplanar spacing is about 0.27 and 0.31 nm respectively, which corresponds to the separation between (104) and (310) lattice planes of Fe_2O_3 and MnO_2. Catalyst containing 20 at% Mn–Fe was chosen as the optimal catalyst. The maximal CO conversion rate was 15%, and the yield of olefins (totally about 23.77%) with a predominance of CH_4 (12.24%), and C_2H_6 (2.80%) components. Mn–Fe catalyst can be regarded as a potential candidate for catalytic conversion of biomass-derived syngas to olefins.

References

[1] R. Snel, Catal. Rev.—Sci. Eng. 29 (1987) 361.
[2] N. Nahon, V. Perrichon, P. Turlier, React. Kinet. Catal. Lett. 12 (1979) 139.
[3] A.P. Steynberg, M.E. Dry, Fischer-Tropsch Technology, Elsevier, Amsterdam, 2004.
[4] A.A. Mirzaei, R. Habibpour, E. Kashi, Appl. Catal. A—Gen. 296 (2005) 222.
[5] Y.J. Lee, J.Y. Park, K.W. Jun, J.W. Bae, N. Viswanadham, Catal. Lett. 126 (2008) 149.
[6] C. Wang, Q. Wang, X. Sun, L. Xu, Catal. Lett. 105 (2005) 93.
[7] J. Barrault, C. Renard, Appl. Catal. 14 (1985) 133.
[8] J. Venter, M. Kaminsky, G.L. Geoffroy, M.A. Vannice, J. Catal. 103 (1987) 450.
[9] Y. Yang, H. Xiang, Y. Xu, L. Bai, Y. Li, Appl. Catal. A—Gen. 266 (2004) 181.
[10] X. Li, B. Zhong, S. Peng, Q. Wang, Catal. Lett. 23 (1994) 245.
[11] L. Xu, Q. Wang, Y. Xu, J. Huang, Catal. Lett. 31 (1995) 253.
[12] S.C. Roy, H.L. Prasad, P. Dutta, A. Bhattacharya, B. Singh, S. Kumar, Appl. Catal. A 220 (2001) 153–164.
[13] S.H. Kang, J.W. Bae, K.J. Woo, P.S. Sai Prasad, K.W. Jun, Fuel Process. Technol. 91 (2010) 399–403.
[14] M. Feyzi, A.A. Mirzaei, J. Nat. Gas Chem. 19 (2010) 422–430.
[15] J.J. Venter, M.A. Vannice, Catal. Lett. 7 (1990) 219–240.
[16] X.G. Li, B. Zhong, S.Y. Peng, Q. Wang, Catal. Lett. 23 (1994) 245–250.
[17] F. Tihay, A.C. Roger, A. Kiennemann, G. Pourroy, Catal. Today 58 (2000) 263–269.
[18] L.Y. Xu, Q.X. Wang, Y.D. Xu, J.S. Huang, Catal. Lett. 31 (1995) 253–266.
[19] S. Li, S. Krishnamoorthy, A. Li, G.D. Meitzner, E. Iglesia, J. Catal. 206 (2002) 202–217.
[20] R.A. Dictor, A.T. Bell, J. Catal. 97 (1986) 121–136.
[21] D.B. Bukur, D. Mukesh, S.A. Patel, Ind. Eng. Chem. Res. 29 (1990) 194–204.
[22] A.A. Ismail, Appl. Catal. B: Env. 58 (2005) 115–121.
[23] D. Patil, V. Patil, P. Patil, Sens. Actuators B 152 (2011) 299.
[24] R. Al-Gaashani, S. Radimana, N. Tabet, A.R. Daud, J. Alloys Compd. 550 (2013) 395–401.
[25] B.J. Tan, K.J. Klabunde, P.M.A. Sherwood, J. Am. Chem. Soc. 113 (1991) 855–861.
[26] M.V. Ananth, S. Pethkar, K. Dakshinamurthi, J. Power Sources 75 (1998) 278–282.
[27] C.M. Julien, M. Massot, C. Poinsignon, Spectrochim. Acta Part A 60 (2004) 689–700.
[28] L. Dghoughi, B. Elidrissi, C. Bernede, M. Addou, M.A. Lamrani, M. Regragui, H. Erguig, Appl. Surf. Sci. 253 (2006) 1823–1829.
[29] N. Ozer, F. Tepehan, Sol. Energy Mater. Sol. Cells 56 (1999) 141–152.
[30] K.M. Reddy, B. Wei, C. Song, Catal. Today 43 (1998) 187–202.